

Asteroseismic Structure Inversions of Main-Sequence Solar-like Oscillators with Convective Cores

LYNN BUCHELE ^{1,2}, EARL P. BELLINGER ³, SASKIA HEKKER ^{1,2} AND SARBANI BASU ³

¹*Heidelberg Institute for Theoretical Studies, Schloss-Wolfsbrunnengasse 35, 69118 Heidelberg, Germany*

²*Center for Astronomy (ZAH/LSW), Heidelberg University, Königstuhl 12, 69117 Heidelberg, Germany*

³*Department of Astronomy, Yale University, PO Box 208181, New Haven, CT 06520-8101, USA*

ABSTRACT

Asteroseismic inferences of main-sequence solar-like oscillators often rely on best-fit models. However, these models cannot fully reproduce the observed mode frequencies, suggesting that the internal structure of the model does not fully match that of the star. Asteroseismic structure inversions provide a way to test the interior of our stellar models. Recently, structure inversion techniques were used to study 12 stars with radiative cores. In this work, we extend that analysis to 43 main-sequence stars with convective cores observed by *Kepler* to look for differences in the sound speed profiles in the inner 30% of the star by radius. For around half of our stars, the structure inversions show that our models reproduce the internal structure of the star, where the inversions are sensitive, within the observational uncertainties. For the stars where our inversions reveal significant differences, we find cases where our model sound speed is too high and cases where our model sound speed is too low. We use the star with the most significant differences to explore several changes to the physics of our model in an attempt to resolve the inferred differences. These changes include using a different overshoot prescription and including the effects of diffusion, gravitational settling, and radiative levitation. We find that the resulting changes to the model structure are too small to resolve the differences shown in our inversions.

1. INTRODUCTION

Among the stars observed by *Kepler*, high-precision oscillation mode frequencies have been determined for around 100 main-sequence solar-like oscillators (Davies et al. 2016; Lund et al. 2017). This sample has been used to study a variety of physical processes including chemical transport (Nsamba et al. 2018; Deal et al. 2018; Verma & Silva Aguirre 2019; Moedas et al. 2022, 2024), convection in stellar cores (Angelou et al. 2020; Zhang 2020; Noll & Deheuvels 2023), rotation (Bétrisey et al. 2023), and magnetic fields (Santos et al. 2018; Salabert et al. 2018; Kiefer & Broomhall 2020). This work often involves finding a best-fit model for each star using a stellar evolution code. Best-fit models are generally found by matching the observed frequencies of a star or by fitting parameters derived from those frequencies, such as the frequency separation ratios (Roxburgh & Vorontsov 2003) or glitch signatures due to helium ionization (Verma et al. 2017), while matching the position of the star on the HR diagram. In general, however, these models are unable to fully reproduce the observed parameters, suggesting that there are still some deficits in our understanding of stellar interiors.

Fortunately, the large number of precise oscillation modes observed in these stars makes it possible to take the analysis further using structure inversions. This technique, developed for geology (Backus & Gilbert 1968) and used extensively in helioseismology (for a review see, for example, Basu 2016; Christensen-Dalsgaard 2021), uses the inherent sensitivity of each oscillation mode to infer differences between the interior structure of a star and a given best-fit model (see e.g. Gough & Thompson 1991; Gough 1993; Pijpers 2006; Bellinger et al. 2020; Buldgen et al. 2022a). These inferred differences can be used to test how well the interior structure of our models matches that of observed stars, as well as provide information on what changes may be necessary to improve our models.

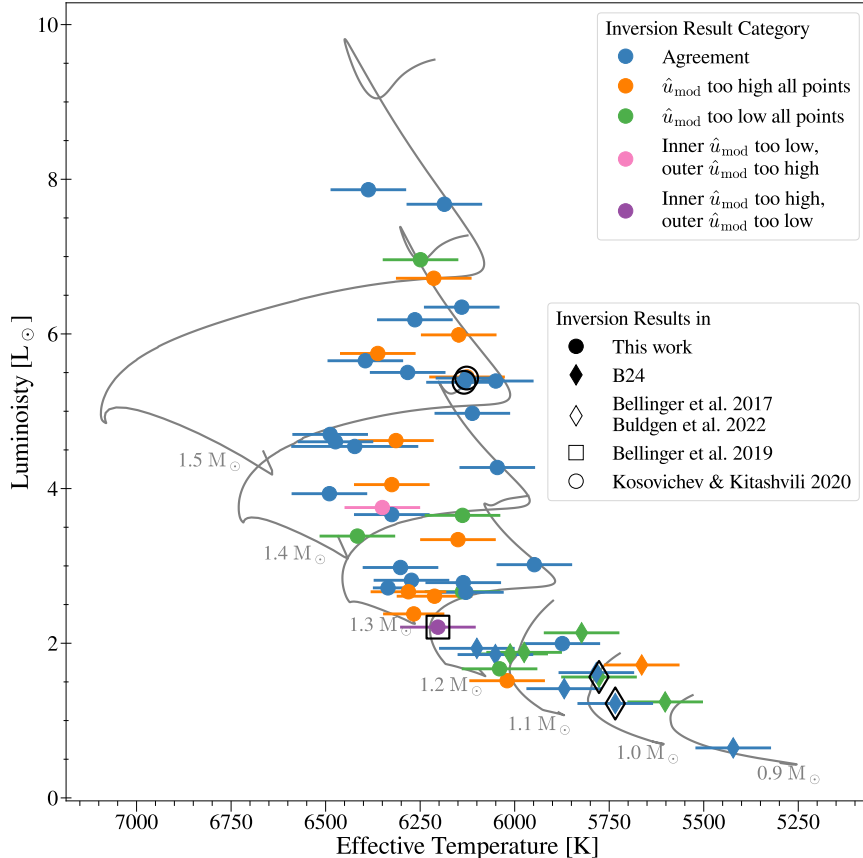


Figure 1. Hertzsprung–Russell diagram for main-sequence solar-like oscillators, with inversion results available. Stars have been categorized based on their inversion results in this work and in B24, represented by the color of the symbol. Stars with other inversion results available are indicated with larger open symbols. The uncertainties of the luminosity values are smaller than the points. Stellar evolutionary tracks of several masses are shown for reference.

In Figure 1, we show the existing sample of main-sequence solar-like oscillators studied using asteroseismic structure inversions. Buchele et al. (2024), henceforth B24, presented results for 12 stars with radiative cores, including the solar analogues 16 Cyg A and B which were also studied by Bellinger et al. (2017) and Buldgen et al. (2022b). Structure inversions have also been used to study a main-sequence star with a small convective core (Bellinger et al. 2019) and two stars evolved enough to exhibit mixed modes (Kosovichev & Kitiashvili 2020). All three of these stars are in the sample presented here, where we extend the work of B24 to cover main-sequence solar-like oscillators with convective cores observed by *Kepler*.

2. FORWARD MODELING

As structure inversions infer differences between a star and a model, the first step is to find a suitably close reference model, typically the best-fit model from a grid-based modeling or optimization procedure. The process of finding such a model is called forward modeling. To find our reference models, we used a grid-based method similar to that used by B24. We constructed a grid of 24,530 tracks using the stellar evolution code MESA (Paxton et al. 2011, 2013, 2015, 2018, 2019; Jermyn et al. 2023). The details of the grid that are unchanged between this work and B24 are detailed in Appendix A.1. There are two important changes which we discuss here. It is well known that including diffusion and gravitational settling of elements without also including the effects of radiative levitation produces models with unrealistic surface abundances in this mass range (e.g. Michaud et al. 2015; Deal et al. 2018). However, including radiative levitation significantly increases the computation time of models, such that it would be difficult to compute the number of models necessary to cover the parameters space of the observations. We chose to compromise and evolve our tracks without including diffusion, settling, or radiative levitation. Additionally, since we are dealing with stars with convective cores, we use the exponential overshooting scheme implemented in MESA where the overshoot region

Table 1. Grid Parameters

Parameter	Minimum Value	Maximum Value
M/M_{\odot}	1.1	1.7
Y_{initial}	0.24	0.4
Z_{initial}	0.0005	0.07
α_{mlt}	1.3	2.4
f_{ov}	0	0.08

is treated as fully mixed without changing the thermal gradient. This is described in detail in Paxton et al. (2011). The parameters varied in this grid are mass, initial helium abundance, initial metallicity, mixing length parameter, and overshooting parameter. To cover the parameter space efficiently, we varied each parameter using a Sobol sequence (see Appendix B of Bellinger et al. 2016; Sobol’ 1967) within the ranges listed in Table 1. For each model in the grid, we calculated the adiabatic frequencies using GYRE (Townsend & Teitler 2013). We then scanned the grid to find the model parameters that best fit the frequencies, effective temperature, and metallicity by minimizing:

$$\chi_{\text{fit}}^2 = \frac{(T_{\text{eff,obs}} - T_{\text{eff,mod}})^2}{\sigma_{T_{\text{eff}}}^2} \quad (1)$$

$$+ \frac{([\text{Fe}/\text{H}]_{\text{obs}} - [\text{Fe}/\text{H}]_{\text{mod}})^2}{\sigma_{[\text{Fe}/\text{H}]}^2} \quad (2)$$

$$+ \frac{1}{N} \sum_i^N \frac{(\nu_{i,\text{obs}} - \nu_{i,\text{mod}})^2}{\sigma_{\nu,i}^2}, \quad (3)$$

where N is the number of observed frequencies, ν_i is the frequency that corresponds to the i th pair of radial order (n) and spherical degree (l) where the model’s frequencies have been corrected for surface effects using the two-term correction from Ball & Gizon (2014), σ denotes the uncertainty of the observed parameter, and the subscripts ‘obs’ and ‘mod’ denote the observations and the model, respectively. Our definition of χ_{fit}^2 treats all the frequencies as a single observation with the same weight as each spectroscopic observation. This choice is common in asteroseismic modeling pipelines (see, for example, the ASTFIT pipeline described in Silva Aguirre et al. 2015). Each mode can be treated as an independent observation by removing the factor of $1/N$. In synthetic tests, Cunha et al. (2021) find that this weighting recovers the correct stellar parameters only when the physics of the grid matches the physics of the synthetic star exactly. As we perform structure inversions in order to determine if the physics in our models accurately represents what we observe, we therefore opt to treat all frequencies as a single observation.

While scanning the grid, we interpolated along each track, but not between tracks. This is the same method as that of B24 with one change — in this work we interpolated in age instead of central hydrogen abundance, as the central hydrogen abundance does not decrease monotonically in stars where a convective core emerges after the zero-age main-sequence. From this procedure, we obtain the best-fit parameters, which are then used to calculate the reference model of the structure inversions. Our values of T_{eff} and $[\text{Fe}/\text{H}]$ come from Furlan et al. (2018); Mathur et al. (2017); Morel et al. (2021), with the specific source for each star given in Appendix A.2. We also provide, in Appendix A.2, the parameters of our best-fit model as well as a comparison to the parameters reported in Silva Aguirre et al. (2017). Additionally, we provide both the FGONG structure file and the inlist used to generate each model at **link to be added upon publication**.

3. STRUCTURE INVERSIONS

With a suitable reference model for each star in our sample, we now turn to the process of an asteroseismic structure inversion. Structure inversions use the frequency differences between a star and its best-fit model to infer the underlying structure differences. We chose to express the structure differences in terms of the dimensionless squared isothermal sound speed (\hat{u}) and helium mass fraction (Y). In terms of the more common structure variables of pressure (P) and

density (ρ),

$$\hat{u} = \frac{P}{\rho} \frac{R}{M} \quad (4)$$

where R and M are the stellar radius and mass, respectively. This choice of variables is well suited for asteroseismic targets (Basu 2003; Bellinger et al. 2020), as the oscillations are mostly insensitive to Y . This makes it easier to isolate the differences due to a change in \hat{u} .

Mathematically, the sensitivity of each mode frequency to a small change in the structure is expressed as:

$$\frac{\delta\hat{\nu}_i}{\hat{\nu}_i} = \int K_i^{(\hat{u}, Y)} \frac{\delta\hat{u}}{\hat{u}} dr + \int K_i^{(Y, \hat{u})} \delta Y dr + \text{higher order terms.} \quad (5)$$

Such an equation can be written for each mode i , where the index i of the mode again corresponds to a specific pair of n, l . The relative frequency difference ($\delta\hat{\nu}_i/\hat{\nu}_i$) is related to the structure differences between the model and the observed star through the mode kernel functions K_i . These mode kernels are known functions of the reference model, found through a linear perturbation of the oscillation equations (for more details, see Gough & Thompson 1991, Kosovichev 1999, or Thompson & Christensen-Dalsgaard 2002). As we are inverting for dimensionless structure variables we need to use the difference in dimensionless frequency ($\hat{\nu}$). These differences are calculated by scaling the dimensional frequency differences by the large frequency separation, $\Delta\nu$:

$$\frac{\delta\hat{\nu}_i}{\hat{\nu}_i} \approx \frac{\Delta\nu_{\text{mod}}}{\Delta\nu_{\text{obs}}} \frac{\nu_{i,\text{obs}}}{\nu_{i,\text{mod}}} - 1. \quad (6)$$

This works because $\Delta\nu$ carries the same dependence on the stellar mass and radius as the frequencies. The full derivation of Equation 6 can be found in Appendix B2 of B24. We note that the model frequencies $\nu_{i,\text{mod}}$ in this expression have been corrected for surface effects using the two-term formulation of Ball & Gizon (2014). We also calculate $\Delta\nu_{\text{mod}}$ after applying the surface term correction.

We choose to correct for dimensional differences and surface effects when calculating the frequency differences. These effects, however, can be handled in different ways. Alternative approaches to handling dimensional differences include using a different correction method (Bellinger et al. 2021), including the mean density in the fitting procedure (Buldgen et al. 2022b), or adding a term to Equation 5 (Kosovichev & Kitiashvili 2020). Following the arguments outlined in Appendix B2 of B24, we expect that the inversion procedure will suppress the effects of differences in mean density regardless of the correction method used. Bellinger et al. (2019) shows this explicitly as inversions using models of different masses and radii return the same results. The surface term can also be accounted for during the inversion by adding a term to Equation 5 (e.g., Equation 3 of Bellinger et al. 2016). We have tested this approach and found no difference in the final inversion results.

If the structure differences are known, then the right-hand side of Equation 5 can be used to calculate the corresponding frequency differences. When comparing an observed star to its best-fit model, however, we know the frequency differences and seek to infer the underlying structure differences. We accomplish this through the method of optimally localized averages (Backus & Gilbert 1968, 1970). This constructs a linear combination of mode kernels that localizes the overall sensitivity around a single target radius, r_0 . Neglecting higher-order effects, Equation 5 becomes:

$$\sum_i^N c_i \frac{\delta\nu_i}{\nu_i} = \int \mathcal{K}_{r_0} \frac{\delta\hat{u}}{\hat{u}} dr + \int \mathcal{C}_{r_0} \delta Y dr. \quad (7)$$

Here c_i are known as the inversion coefficients, $\mathcal{K} = \sum_i^N c_i K_i^{(\hat{u}, Y)}$ is called the averaging kernel, and $\mathcal{C} = \sum_i^N c_i K_i^{(Y, \hat{u})}$ is the cross-term kernel. When the inversion coefficients are chosen such that \mathcal{K} is localized around r_0 and normalized to 1, and the amplitude of \mathcal{C} is small everywhere, then Equation 7 reduces to

$$\sum_i^N c_i \frac{\delta\nu_i}{\nu_i} \approx \int \mathcal{K}_{r_0} \frac{\delta\hat{u}}{\hat{u}} dr \approx \left\langle \frac{\delta\hat{u}}{\hat{u}} \right\rangle_{r_0}. \quad (8)$$

Thus once the inversion coefficients are known, the sum on the left-hand side provides a localized average of the difference in \hat{u} around r_0 .

Table 2. Stars with Mixed Modes Removed

KIC Number	Number of $l = 2$ modes removed
8228742	3
7940546	3
10068307	4
12317678	1
3632418	1
10162436	1
9353712	1
9414417	1
3456181	1
12069127	2
6679371	2

To find the inversion coefficients, we used the method of multiplicative optimally localized averages (MOLA), which constructs the averaging kernel by penalizing any amplitude away from the target radius. For details on the implementation of MOLA, see [Basu & Chaplin \(2017, Chapter 10\)](#). In this process, we must choose two trade-off parameters: β , the cross-term suppression parameter, and μ , the error suppression parameter. We chose our parameter values using the same method as B24. Briefly, this method sets $\beta = 0$ as the choice of Y as the second variable naturally suppresses the amplitude of the cross-term kernel. We then chose a value of μ that could correctly recover the known values of $\delta\hat{u}/\hat{u}$ between our reference model and a small set of calibration models. These models came from our grid and have slightly larger values of χ_{fit}^2 than our reference model.

For each target star, we attempted to construct an averaging kernel for six target radii: $r_0/R = 0.05, 0.1, 0.15, 0.2, 0.25, 0.3$. In general, the presence of a convective core made it more difficult to localize sensitivity at target radii close to the boundary of the core, and so in most cases the innermost target radius we report is $r_0/R = 0.15$. It is possible that frequencies derived from radial velocity measurements instead of photometric measurements could expand this range by providing more modes overall, which would help to suppress the sensitivity to the boundary of the convective core, and by providing more $l = 3$ modes which make it easier to localize averaging kernels at larger target radii. The uncertainties of our inversion results are calculated using a Monty Carlo simulation to account for possible error correlations introduced by our corrections for the mean density and surface effect (for the specific details, see B24). We also report the FWHM of each averaging kernel as a measure of the resolution of each inversion.

For 11 stars, our models showed that the lowest order quadrupole modes were mixed acoustic-buoyancy modes. We have found that current linear inversion techniques are not suitable for mixed-modes ([Buchele et al., in preparation](#)) and hence, while we accounted for these mixed modes when fitting our models, we removed these modes from the mode set used for the structure inversions. [Table 2](#) shows the stars with mixed modes present and how many quadrupole modes were excluded from our inversions.

4. RESULTS

We divide our 43 stars into five categories based on their inversion results: (A) stars with no significant disagreement in the region probed by inversions, (H) stars for which all significant differences show that the model \hat{u} is too high, (L) stars for which all significant differences show the model \hat{u} is too low, (LH) stars where the model \hat{u} is too low in the center and too high in the outer points probed by the inversions, and (HL) stars where the model \hat{u} is too high in the center and too low in the outer points probed by the inversions. In [Figure 2](#), we show an example of inversion results from one star in each category.

Around half (24) of the stars fall into category (A). These models still show significant differences in the oscillation frequencies, even after correcting for the surface term, which suggests that the structure differences are either smaller

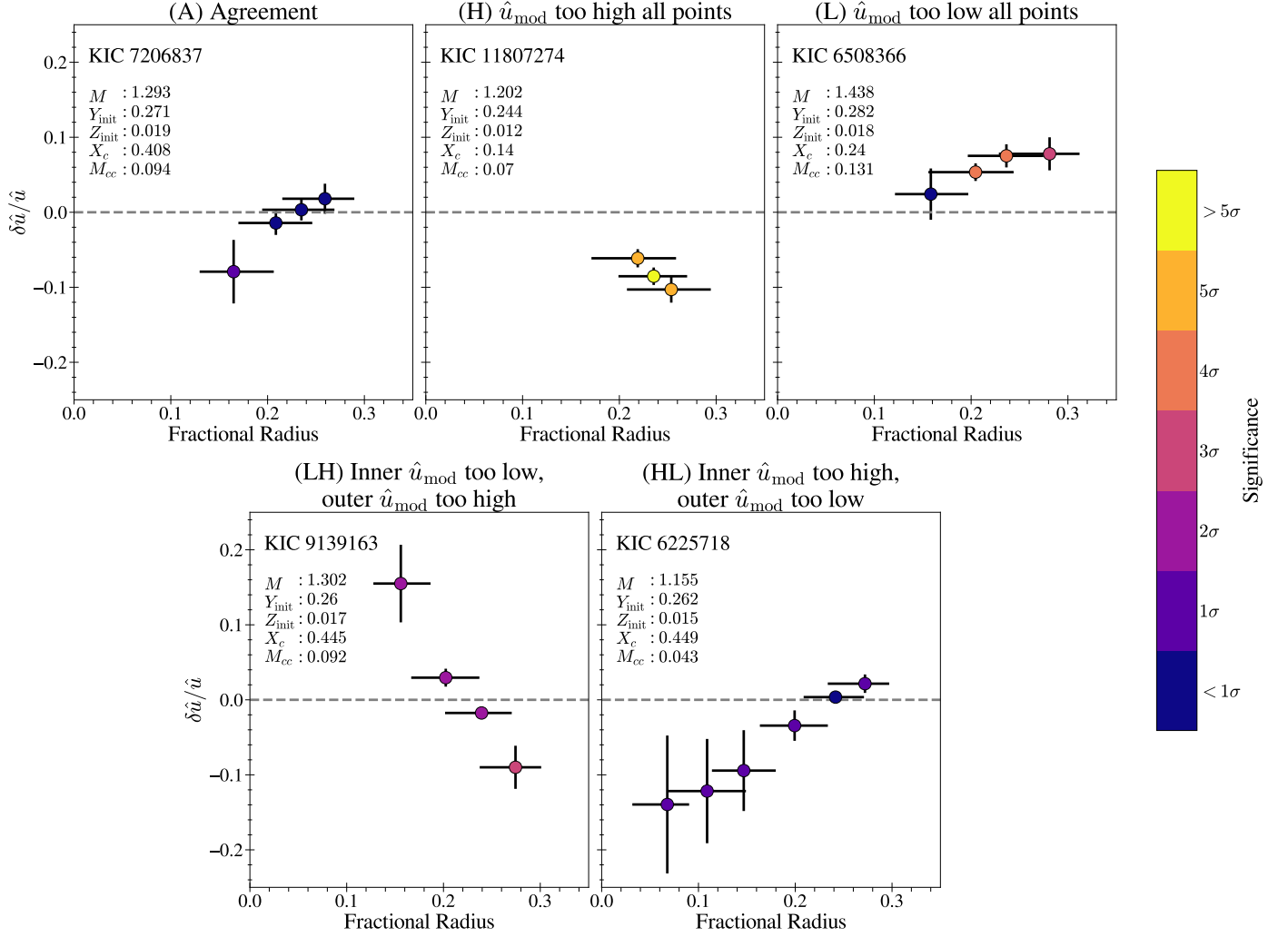


Figure 2. Inversion results for one star in each category. Each shows the relative differences in \hat{u} between observation and best-fit model inferred by the inversions, in the sense of $(\text{Star} - \text{Model})/\text{Model}$. The vertical error bars indicate the uncertainty of each inversion result from the propagation of the uncertainty of the observed frequencies. The horizontal error bars represent the full width at half maximum of the averaging kernel. The dashed horizontal line indicates complete agreement between the model and observations; points above this line imply that \hat{u} of the star is larger than that of the model. The color bar indicates the statistical significance of the inferred difference, with lighter colors showing more significant results. We also provide the mass (M , in M_{\odot}), initial helium mass fraction (Y_{init}), initial metallicity (Z_{init}), central hydrogen mass fraction (X_c), and mass of the convective core (M_{cc} , in M_{\odot}) of each model.

than the observational uncertainties at the resolution given by the structure inversions or that the structure differences are at a location unable to be probed by the inversions. Of the stars showing significant disagreement, 11 are in category (H), 6 are in category (L), and 1 each in categories (LH) and (HL). Using the χ_{inv}^2 parameter defined in B24, we search for correlations with a variety of model parameters and observations. In contrast to the earlier work, we find no significant correlations. One problem with the χ_{inv}^2 metric is that it only measures the significance of the inversion results, not whether the differences inferred are positive or negative. To account for this, we also look for correlations between the model parameters and $a\chi_{\text{inv}}^2$ where $a = -1(+1)$ for stars where the most significant inferred difference is negative (positive). We also find no significant correlations in this case.

For 13 stars, we find models with both convective and radiative cores in our calibration set. In general, the models of the stars that do have convective cores have small ones, implying the structure differences between the calibration models are relatively small. The distribution of the inversion results within this subsample is similar to that of the

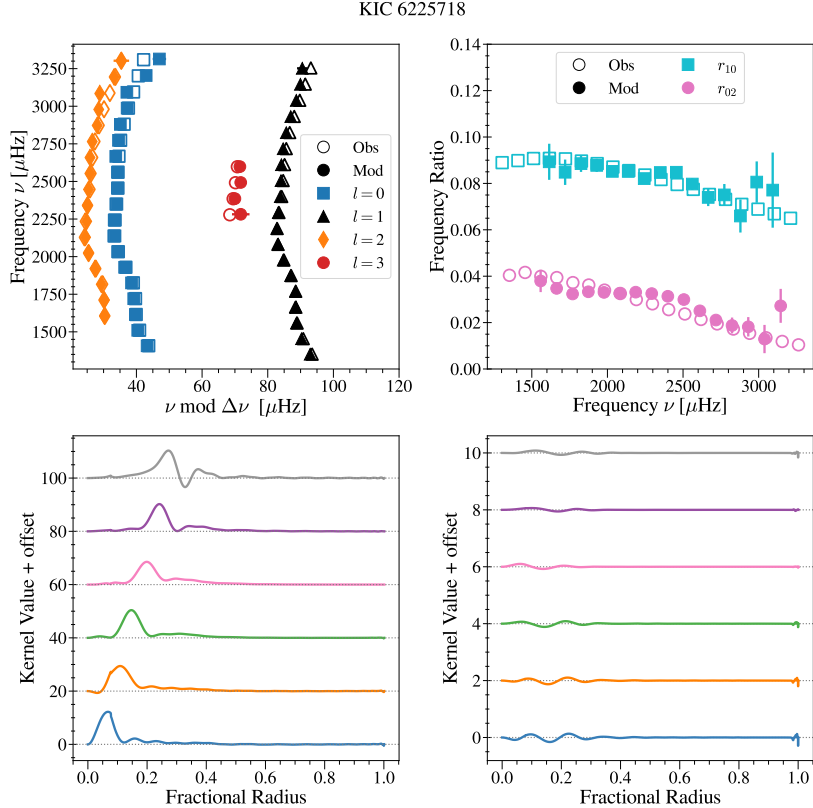


Figure 3. Information about the best-fit model of KIC 6225718. The top left plot shows the frequency échelle diagram comparing the frequencies of the reference model to the observations after correcting for surface effects. The top right plot shows the frequency separation ratios of the reference model and observations. The ratios of the reference model have been computed from the uncorrected model frequencies. The bottom left plot shows the averaging kernels and the bottom right the cross-term kernels. Note that the y -axis scale differs by an order of magnitude between the two plots on the bottom row.

whole sample, suggesting that the differences we infer are not due to the ambiguity in whether the core is convective or radiative.

We discuss here only a few of our 43 stars, focusing on the stars that other works have also analyzed with structure inversions. We present the full inversion results for each star in Appendix B.

4.1. KIC 6225718

The first star we discuss in detail is KIC 6225718. Our inversion results for this star are shown in Figure 2. We show in Figure 3 the frequency échelle diagram and frequency separation ratios of our best-fit model, as well as, our averaging and cross-term kernels. This star has already been studied using structure inversions by Bellinger et al. (2019) which allows us to compare our results. Structure inversions infer differences relative to a given reference model using a given set of averaging kernels. As such, any comparison of different inversion results must be considered in the context of the reference model and averaging kernels used. The averaging kernels we use are very similar to those used in Bellinger et al. (2019). In comparing the structure of our reference model to the original model used by Bellinger et al. (2019), we find that ours has a slightly larger convective core (with our convective boundary located at $r/R \approx 0.08$ instead of $r/R \approx 0.04$). We attribute this difference to our inclusion of core overshoot. Bellinger et al. (2019) also constructed a model with core overshoot which resulted in a convective core boundary closer to our reference model. The inversion results for this model are not reported, however, the authors note that the inversion results were the same as their original model. Thus we conclude that our inversion results can be directly compared to those in Bellinger et al. (2019).

Both works find that the model \hat{u} is too low in the outermost regions probed by inversions and too high in the innermost regions, with the crossover occurring around $r/R \approx 0.25$. Bellinger et al. (2019) find a maximum difference at $r/R \approx 0.1$, while our maximum difference is found around $r/R \approx 0.05$. However, the higher uncertainties at these

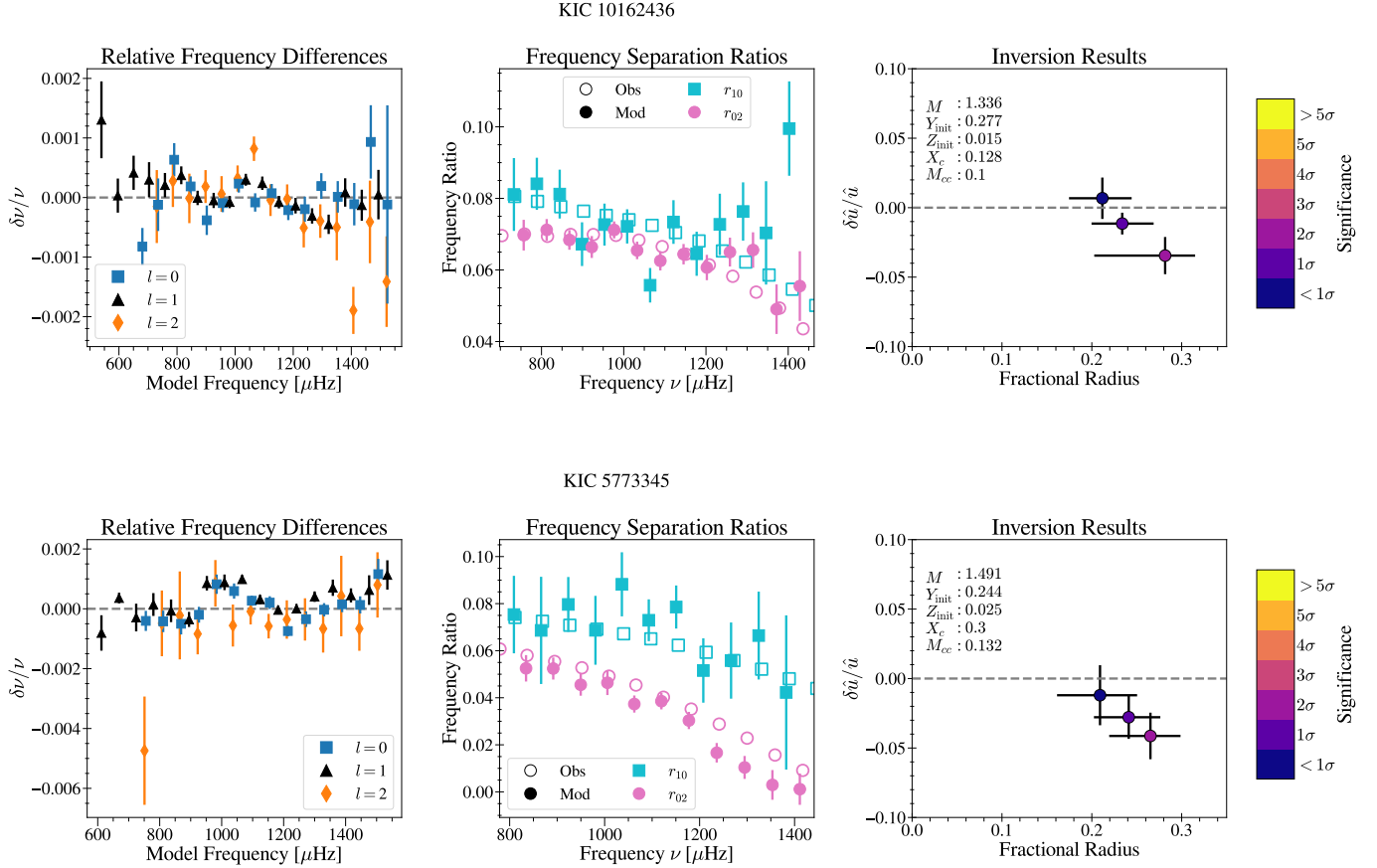


Figure 4. Frequency differences, frequency separation ratios, and inversion results for our models of the two stars shown in [Kosovichev & Kitiashvili \(2020\)](#). The top row shows the results for KIC 10162436. The figure on the left shows the relative frequency differences, after correcting for surface effects. The center panel shows the frequency separation ratios of the observed star and our reference model (computed using uncorrected model frequencies). The right panel shows the inversion results, where all symbols and colors have the same meaning as in [Figure 2](#). The lower row shows the same information for KIC 5773345.

target radii mean that this difference in inversion results is not significant. Thus, despite slight differences in the fitting and inversion procedures, we find the same disagreement in internal structure.

4.2. KIC 10162436 and KIC 5773345

[Kosovichev & Kitiashvili \(2020\)](#) present inversion results for two stars that are also in our sample: KIC 10162436 and KIC 5773345. Our results for these stars are shown in [Figure 4](#). Directly comparing our inversion results to theirs is slightly more difficult than with [Bellinger et al. \(2019\)](#). For both stars, they find mixed modes with $l = 1$ and $l = 2$. Our model of KIC 10162436 has one mixed $l = 2$ mode, which we exclude from our inversions, and no $l = 1$ mixed mode. In the case of KIC 5773345, our model shows no mixed modes at all. In addition, the frequency differences, even of pure acoustic modes, between their models and the observations are significantly larger than ours. These differences in frequencies and mode character, which we attribute to differences in the modeling procedure¹, suggest that the structure of the reference models used in [Kosovichev & Kitiashvili \(2020\)](#) and this work are different. Additionally, while [Kosovichev & Kitiashvili \(2020\)](#) do not show their averaging kernels, the spread indicated by their horizontal error bars are much wider than ours. Thus we cannot directly compare our inversion results to those given

¹ [Kosovichev & Kitiashvili \(2020\)](#) use the parameters from the YCMC modeling pipeline presented in [Silva Aguirre et al. \(2017\)](#), including the mixing length parameter and stellar age, to compute a model using MESA. However, the default nuclear reaction rates and formulation of mixing length theory implemented in MESA differ from those used in the YCMC models. It is unclear if the MESA defaults were changed to match the physics used in the YCMC models. If these changes were not made the YCMC parameters may not result in a best-fit model.

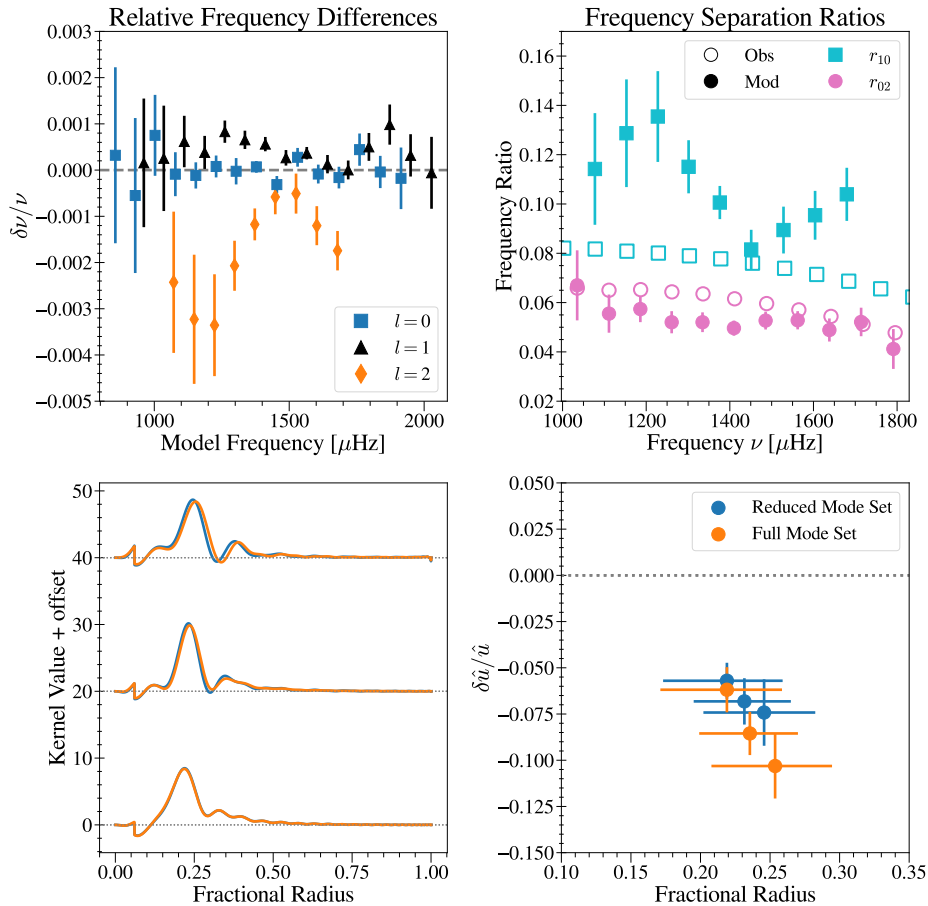


Figure 5. Results of the modeling and modeset testing of KIC 11807274. The top-left figure shows the relative frequency differences, after correcting for surface effects. The top-right figure shows the frequency separation ratios of the observed star and our reference model (computed using uncorrected model frequencies). The bottom right figure shows the original averaging kernels and those constructed when excluding the three lowest frequencies $l = 2$ modes. The bottom left figure shows the results of inversions using each mode set.

in [Kosovichev & Kitiashvili \(2020\)](#). Nevertheless, we note that we infer differences in \hat{u} of similar magnitude for both KIC 10162436 and KIC 5773345.

4.3. KIC 11807274

We now turn to the star with the most significant differences inferred by our inversions, KIC 11807274. We show in Figure 5 the frequency differences and frequency separation ratios for this star. Our reference model is in full agreement with the observed values of T_{eff} and $[\text{Fe}/\text{H}]$. The largest frequency differences are seen in the lower order quadrupole frequencies, which exhibit a glitch structure not reproduced in any model. To understand how sensitive our results are to these discrepant frequencies, we repeat both our modeling and inversion procedure excluding the lowest three quadrupole models. Our fitting procedure results in the same model as we found using the entire mode set. We show the averaging kernels and inversion results of the reduced mode set compared with the full mode set in Figure 5. Removing these modes results in slightly different averaging kernels, most notably for the highest target radius, where the maximum of kernel amplitude is shifted towards the center of the star. The differences inferred with these new averaging kernels are smaller than with the full mode set, however significant differences remain.

4.4. Changes in Input Physics

We now explore several changes to the physics of our models as a first step to resolve the differences inferred by structure inversions. As a full study of all possible changes to all the stars is beyond the scope of this work, we focus only on the star with the most significant differences revealed by our inversions, KIC 11807274. The inversion results

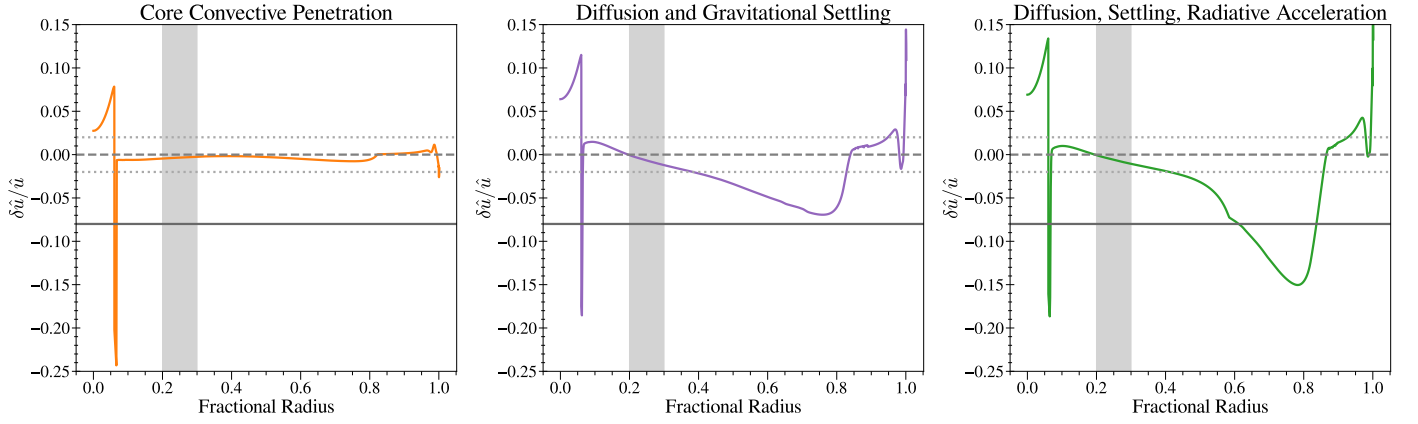


Figure 6. Results of varying the several mixing processes for models of KIC 11807274. Each plot shows the relative difference in \hat{u} between our original reference model and a model with different physics. We indicate 0 with a dashed horizontal line, the uncertainties of our inversion with dotted horizontal lines, and indicate the inferred difference at our middle target radius with the solid horizontal line. The vertical shading indicates the fractional radii where our inversions are sensitive. In all three panels, the spike around $r/R \approx 0.1$ is due to differences in the boundary of the convective core. The larger changes in the center and right panels around $r/R \approx 0.8$ are due to differences in the depth of the outer convection zone.

are shown in Figure 2. In Figure 6, we show the changes to the \hat{u} profile that result from three different changes to the physics. The first change we present is a change to core boundary mixing. Instead of calculating the overshoot using exponential overmixing, where only the composition of the overshooting region is changed, this model uses a step convective penetration scheme described in Appendix A.1, where both the composition and the temperature gradient are changed in the overshoot region. For this change, we find new model parameters from a new grid created with the changed overshooting scheme. This change results in a slightly larger convective core, which causes the spike in the relative difference around $r/R \approx 0.05$. Otherwise, the main difference in the \hat{u} profile is within the convective core, below the radius where our inversions probe. In the region where our inversions are sensitive, the change to \hat{u} is in the correct direction according to our inversion results, but it is far too small to resolve the differences. In fact, the change is smaller than the uncertainties of our inversions. Several works (Lebreton & Goupil 2012; Deal et al. 2023) have suggested that a large amount of convective penetration at the base of the outer convection zone may explain glitches observed in the frequency separation ratios of F-type stars. We have tested this prescription as well and find a change to the \hat{u} at the base of the convective envelope $r/R \sim 0.8$, but at the radius where our inversions are sensitive the structure is very similar to the model without this additional mixing. Hence, this change is unable to resolve the differences inferred by our inversions.

The other changes we examined deal with the transport of chemical elements. We tested the effects of including element diffusion and gravitational settling only as well as accounting for diffusion, settling, and radiative levitation. For both of these models we kept the same overshoot implementation and initial parameters as our original reference model, although we used the age that best fit the observations. In the model including only diffusion and settling we used the inlist parameters of the `diffusion_smoothness` test suite case in MESA. In the model including diffusion, settling, and radiative levitation we adopt the MESA settings of the A0 model in Campilho et al. (2022). In both of the new models we find the largest differences around the base of the convection zone where the transport processes have made the convection zone deeper. In the regions probed by our inversions, however, the changes are small enough to be within the uncertainties of our inversion results.

5. CONCLUSIONS

In this work, we have extended the analysis from Buchele et al. (2024) (B24) to stars with convective cores. We found best-fit models from a grid of tracks computed with MESA by fitting the observed frequencies, effective temperatures, and metallicities. Using each of these best-fit models, we performed structure inversions to compare the internal structure of the model to that of the star. These results, combined with the results of B24, show that our models reproduce the internal structure of around half of the stars examined. In cases where we find significant differences, we see an even split between models with dimensionless squared isothermal sound speed that is higher than the star and cases where it is too low. In contrast to the results of the stars with radiative cores, we did not find any significant

correlations with the properties of our reference models. We tested several changes to the physics in our models and found that the resulting changes to the model structure are much smaller than necessary to reproduce the structure inferred by our inversions.

In both B24 and this work, the structure differences inferred by inversions remain unexplained. In future work, we plan to test potential modifications to the physical ingredients in our stellar modeling using structure inversions. With these changes we aim to consistently improve our models of the stars with significant differences without introducing discrepancies for the stars we currently model well.

The research leading to the presented results has received funding from the ERC Consolidator Grant DipolarSound (grant agreement #101000296). SB acknowledges NSF grant AST-2205026. This paper includes data collected by the Kepler mission. Funding for the Kepler mission is provided by the NASA Science Mission Directorate. In addition, this work has made use of data from the European Space Agency (ESA) mission *Gaia* (<https://www.cosmos.esa.int/gaia>), processed by the *Gaia* Data Processing and Analysis Consortium (DPAC, <https://www.cosmos.esa.int/web/gaia/dpac/consortium>). Funding for the DPAC has been provided by national institutions, in particular the institutions participating in the *Gaia* Multilateral Agreement. We have also used the *gaia-kepler.fun* crossmatch database created by Megan Bedell.

APPENDIX

A. APPENDIX MODELING DETAILS

A.1. *Model Grids*

Here, we provide more details about the grid used to find our reference models. We use metal abundances scaled to the GS98 solar composition (Grevesse & Sauval 1998), and the corresponding high-temperature opacity tables from OPAL (Iglesias & Rogers 1993, 1996), and low-temperature opacity tables from Ferguson et al. (2005). We blend the equation of state data from OPAL (Rogers & Nayfonov 2002), SCVH (Saumon et al. 1995), FreeEOS (Irwin 2004), and Skye (Jermyn et al. 2021) with the default settings. This blending is described in more detail in Jermyn et al. (2022). Our nuclear reaction network is `pp_cno_extras_o18_ne22.net` and we use reaction rates from JINA REACLIB (Cyburt et al. 2010) and NACRE (Angulo et al. 1999), with additional tabulated weak reaction rates (Fuller et al. 1985; Oda et al. 1994; Langanke & Martínez-Pinedo 2000). Electron screening is included via the prescription of Chugunov et al. (2007). Thermal neutrino loss rates are from Itoh et al. (1996). We use the time-dependent local convection formalism of Kuhfuss (1986), which, as described in Jermyn et al. (2022), refuses in the limit of long time steps to standard mixing length theory as described in Cox & Giuli (1968). We use an Eddington-gray atmosphere and include the structure of the atmosphere out to an optical depth of $\tau = 10^{-3}$ when calculating both our oscillation frequencies and structure kernels.

A.1.1. *Convective Penetration*

As MESA does not implement convective penetration by default, we make use of the `other_after_set_mixing_info` hook in `run_star_extras`. This allows us to use MESA’s procedure for calculating the extent of step overshooting region and simply change the temperature gradient after these regions have been identified. It also simplifies the process of including overshoot from the convective core and at the base of the outer convection zone. We include our routine for this at the Zenodo link provided in Section 2.

A.2. *Modeling Information*

In Table 3, we provide the non-seismic constraints used in our modeling procedure. For all but three stars, we take our spectroscopic measurements from Furlan et al. (Table 9 of 2018) and adopt their suggested uncertainties of 100K and 0.1 dex for T_{eff} and $[\text{Fe}/\text{H}]$, respectively. Two of our stars, KIC 434952 and KIC 5773345, are not analyzed by Furlan et al. (2018). In these cases, we use the values from Mathur et al. (2017). The values in Furlan et al. (2018) for KIC 9965715 were found to be discrepant from other literature values, so instead we use the measurements from Morel et al. (2021). To reduce the computation time when finding a best-fit model, we calculate χ^2_{fit} only for models within 6σ of the observed effective temperature and metallicity and 10σ of the observed luminosity. We primarily use the

FLAME luminosity value from Gaia DR3 (Gaia Collaboration et al. 2016; Creevey et al. 2023; Creevey et al. 2023), although some stars are only available in Gaia DR2 (Gaia Collaboration et al. 2018), or not at all.

Table 4 provides the parameters of our reference model for each star and the star’s category based on our inversion results as defined in Section 4. We compare our stellar parameters to those reported in Silva Aguirre et al. (2017) in Figure 7. In general, our values of mass and radius fall within the spread of values in Silva Aguirre et al. (2017) without any clear biases. Our models tend to show higher initial hydrogen mass fraction and lower initial helium mass fraction. We attribute this to our choice not to include diffusion in our models.

B. ALL INVERSION RESULTS

We provide plots that show the frequency differences, separation ratios, averaging kernels, cross-term kernels, and inversion results. In Figure 8 we show as an example KIC 1435467 with the results of all stars available in the online journal.

Fig. Set 8. Modeling and Inversion Results – will be available in the online journal version

Table 3. Non-seismic observations

Star	T_{eff} [K]	[Fe/H]	L [L_{\odot}]
KIC 1435467	6325.0±100.0 ^a	0.04±0.1 ^a	4.051±0.073 ^d
KIC 2837475	6488.0±100.0 ^a	-0.07±0.1 ^a	4.7±0.019 ^d
KIC 3456181	6214.0±100.0 ^a	-0.26±0.1 ^a	6.72±0.04 ^d
KIC 3632418	6112.0±100.0 ^a	-0.16±0.1 ^a	4.973±0.073 ^d
KIC 4349452	6267.0±81.0 ^b	-0.06±0.15 ^b	2.379±0.015 ^d
KIC 5184732	5874.0±100.0 ^a	0.41±0.1 ^a	1.995±0.008 ^d
KIC 5773345	6127.0±82.0 ^b	0.21±0.1 ^b	5.429±0.03 ^d
KIC 5866724	6138.0±100.0 ^a	0.14±0.1 ^a	2.667±0.017 ^d
KIC 6225718	6203.0±100.0 ^a	-0.12±0.1 ^a	2.208±0.007 ^d
KIC 6508366	6249.0±100.0 ^a	-0.06±0.1 ^a	6.959±0.031 ^d
KIC 6679371	6387.0±100.0 ^a	-0.04±0.1 ^a	7.865±0.036 ^d
KIC 7103006	6362.0±100.0 ^a	0.05±0.1 ^a	5.747±0.019 ^d
KIC 7206837	6325.0±100.0 ^a	0.12±0.1 ^a	3.664±0.022 ^d
KIC 7510397	6109.0±100.0 ^a	-0.25±0.1 ^a	...
KIC 7670943	6302.0±100.0 ^a	0.01±0.1 ^a	2.98±0.041 ^d
KIC 7771282	6138.0±100.0 ^a	-0.07±0.1 ^a	3.654±0.029 ^d
KIC 7940546	6126.0±100.0 ^a	-0.27±0.1 ^a	5.443±0.059 ^d
KIC 8179536	6281.0±100.0 ^a	-0.04±0.1 ^a	2.666±0.015 ^d
KIC 8228742	6046.0±100.0 ^a	-0.09±0.1 ^a	4.273±0.042 ^d
KIC 8292840	6212.0±100.0 ^a	-0.21±0.1 ^a	2.608±0.054 ^d
KIC 8379927	6022.0±77.0 ^b	-0.24±0.35 ^b	...
KIC 8866102	6273.0±100.0 ^a	-0.09±0.1 ^a	2.814±0.013 ^d
KIC 9139151	6040.0±100.0 ^a	0.04±0.1 ^a	1.669±0.007 ^d
KIC 9139163	6350.0±100.0 ^a	0.09±0.1 ^a	3.755±0.028 ^d
KIC 9206432	6490.0±100.0 ^a	0.17±0.1 ^a	3.934±0.029 ^d
KIC 9353712	6140.0±100.0 ^a	-0.09±0.1 ^a	6.346±0.057 ^d
KIC 9414417	6283.0±100.0 ^a	-0.09±0.1 ^a	5.502±0.024 ^d
KIC 9592705	6148.0±100.0 ^a	0.27±0.1 ^a	5.987±0.098 ^d
KIC 9812850	6314.0±100.0 ^a	-0.18±0.1 ^a	4.621±0.021 ^d
KIC 9965715	6335.0±40.0 ^c	0.29±0.04 ^c	2.716±0.042 ^d
KIC 10068307	6050.0±100.0 ^a	-0.21±0.1 ^a	5.391±0.021 ^d
KIC 10162436	6134.0±100.0 ^a	-0.14±0.1 ^a	5.374±0.019 ^d
KIC 10454113	6136.0±100.0 ^a	-0.07±0.1 ^a	2.784±0.046 ^d
KIC 10644253	6020.0±100.0 ^a	0.09±0.1 ^a	1.515±0.006 ^d
KIC 10666592	6264.0±100.0 ^a	0.01±0.1 ^a	6.183±0.081 ^e
KIC 10730618	6423.0±168.0 ^b	-0.16±0.3 ^b	4.545±0.04 ^d
KIC 11081729	6416.0±100.0 ^a	-0.13±0.1 ^a	3.386±0.054 ^d
KIC 11253226	6474.0±100.0 ^a	-0.19±0.1 ^a	4.605±0.032 ^d
KIC 11807274	6150.0±100.0 ^a	-0.12±0.1 ^a	3.34±0.027 ^d
KIC 12009504	6129.0±100.0 ^a	-0.08±0.1 ^a	2.659±0.009 ^d
KIC 12069127	6186.0±100.0 ^a	0.03±0.1 ^a	7.677±0.082 ^d
KIC 12258514	5948.0±100.0 ^a	0.01±0.1 ^a	3.016±0.009 ^d
KIC 12317678	6395.0±100.0 ^a	-0.42±0.1 ^a	5.653±0.091 ^e

References—(a) Furlan et al. (2018), (b) Mathur et al. (2017), (c) Morel et al. (2021), (d) Creevey et al. (2023), (e) Gaia Collaboration et al. (2018)

Table 4. Reference Model Parameters

Star	$M[M_{\odot}]$	Y_{initial}	Z_{initial}	α_{mlt}	f_{ov}	X_c	χ_{fit}^2	Inversion Results Category
KIC 1435467	1.3540	0.2794	0.0209	2.2396	0.0231	0.2689	2.32	H
KIC 2837475	1.3297	0.2584	0.0123	2.1497	0.0243	0.4000	7.2	A
KIC 3456181	1.3165	0.2736	0.0104	2.2254	0.0504	0.2191	6.1	H
KIC 3632418	1.2773	0.2496	0.0116	1.9093	0.0219	0.1037	2.29	A
KIC 4349452	1.1394	0.2867	0.0166	2.0684	0.0344	0.3853	1.13	H
KIC 5184732	1.1683	0.3309	0.0399	2.2366	0.0124	0.1589	27.77	A
KIC 5773345	1.4914	0.2443	0.0254	2.0132	0.0464	0.2997	3.8	A
KIC 5866724	1.2668	0.2619	0.0235	2.1377	0.0250	0.3511	1.82	L
KIC 6225718	1.1553	0.2617	0.0147	2.3102	0.0392	0.4493	7.73	HL
KIC 6508366	1.4378	0.2824	0.0175	2.1715	0.0394	0.2403	5.88	L
KIC 6679371	1.5490	0.2421	0.0140	2.1485	0.0110	0.1463	4.38	A
KIC 7103006	1.4718	0.2541	0.0192	2.1252	0.0294	0.3029	1.49	H
KIC 7206837	1.2928	0.2711	0.0191	1.9863	0.0355	0.4079	2.27	A
KIC 7510397	1.3352	0.2438	0.0134	2.1562	0.0168	0.0838	5.46	A
KIC 7670943	1.2531	0.2456	0.0169	2.3065	0.0165	0.2911	1.62	A
KIC 7771282	1.2384	0.2417	0.0137	2.0294	0.0401	0.2714	1.85	L
KIC 7940546	1.3297	0.2584	0.0123	2.1497	0.0243	0.1338	7.97	H
KIC 8179536	1.2186	0.2677	0.0174	2.1525	0.0329	0.4253	3.1	H
KIC 8228742	1.2124	0.2791	0.0128	2.1034	0.0261	0.0278	3.35	A
KIC 8292840	1.1336	0.2461	0.0099	1.9458	0.0127	0.1372	2.28	H
KIC 8379927	1.2308	0.2483	0.0259	2.1166	0.0085	0.5646	6.51	L
KIC 8866102	1.2175	0.2505	0.0139	2.1005	0.0026	0.2313	2.06	A
KIC 9139151	1.1872	0.2655	0.0240	2.3548	0.0143	0.4026	4.92	L
KIC 9139163	1.3016	0.2601	0.0167	2.0525	0.0370	0.4446	5.65	LH
KIC 9206432	1.3915	0.2849	0.0245	2.0034	0.0062	0.5158	4.49	A
KIC 9353712	1.4165	0.2483	0.0149	2.0718	0.0390	0.2046	1.94	A
KIC 9414417	1.3359	0.2789	0.0135	2.3704	0.0200	0.1195	2.79	A
KIC 9592705	1.4472	0.3096	0.0262	2.0641	0.0135	0.0848	3.29	H
KIC 9812850	1.2289	0.2637	0.0106	2.1612	0.0590	0.2986	1.27	H
KIC 9965715	1.2133	0.3272	0.0273	1.9746	0.0147	0.4504	20.35	A
KIC 10068307	1.3505	0.2640	0.0151	2.2139	0.0354	0.0988	7.49	A
KIC 10162436	1.3365	0.2766	0.0149	2.1053	0.0276	0.1281	3.87	A
KIC 10454113	1.2531	0.2456	0.0169	2.3065	0.0165	0.4990	9.16	A
KIC 10644253	1.2308	0.2483	0.0259	2.1166	0.0085	0.6138	2.5	H
KIC 10666592	1.5095	0.2403	0.0193	2.0247	0.0130	0.2321	1.86	A
KIC 10730618	1.2735	0.2600	0.0110	2.2181	0.0435	0.2946	3.46	A
KIC 11081729	1.1776	0.2775	0.0126	1.9915	0.0186	0.3516	4.65	L
KIC 11253226	1.3502	0.2450	0.0129	2.0507	0.0410	0.4803	7.3	A
KIC 11807274	1.2015	0.2445	0.0120	2.1044	0.0203	0.1399	3.65	H
KIC 12009504	1.1244	0.2856	0.0140	2.1580	0.0232	0.2365	4.7	A
KIC 12069127	1.5569	0.2474	0.0173	2.0223	0.0103	0.0847	1.8	A
KIC 12258514	1.1489	0.2656	0.0127	2.1986	0.0307	0.0890	10.74	A
KIC 12317678	1.2723	0.2517	0.0077	1.9616	0.0089	0.0771	4.0	A

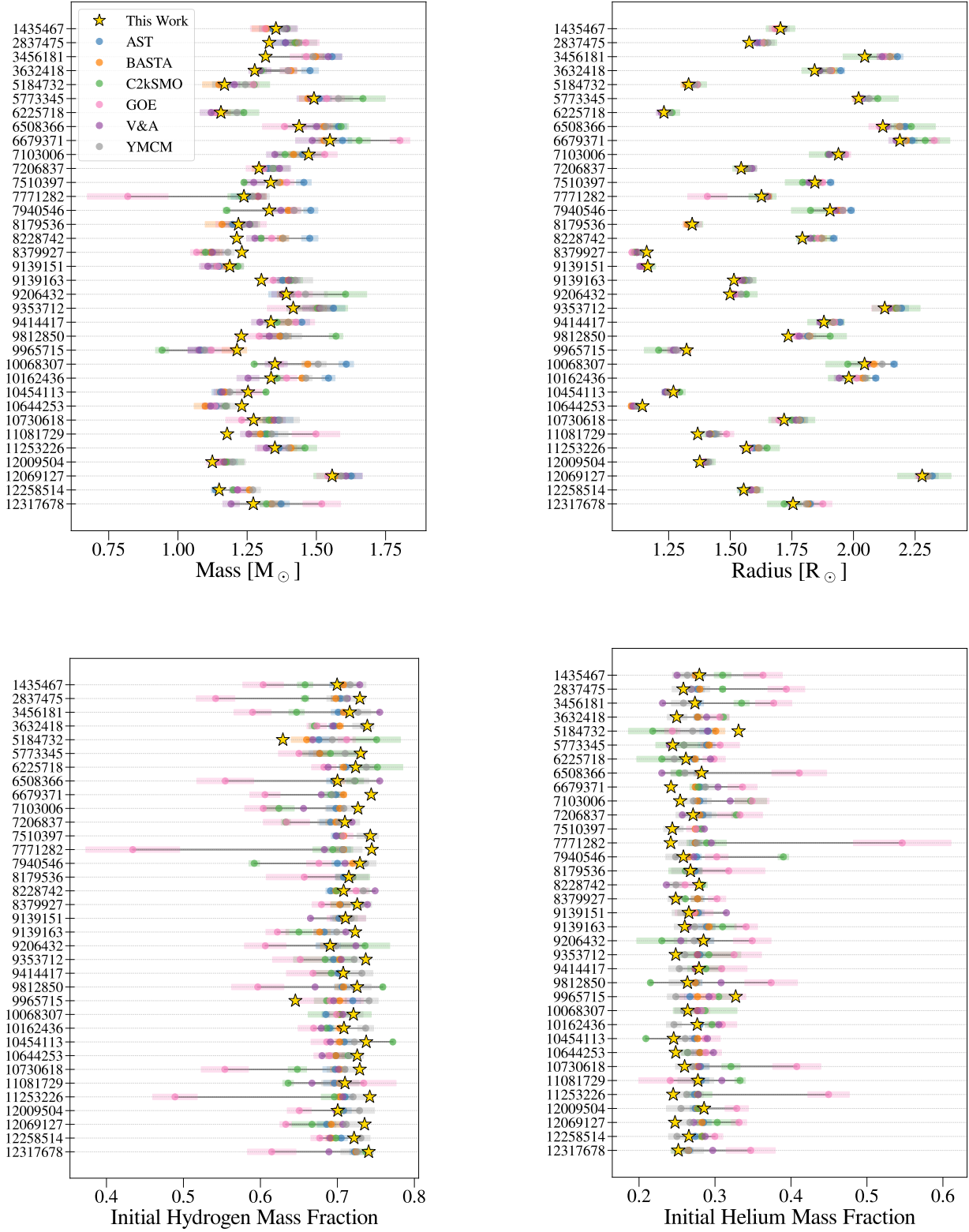


Figure 7. Comparison of our model parameters to several pipelines used in [Silva Aguirre et al. \(2017\)](#). The results of each pipeline are indicated with a dot and the uncertainties of that result are indicated by a shaded region of the same color.

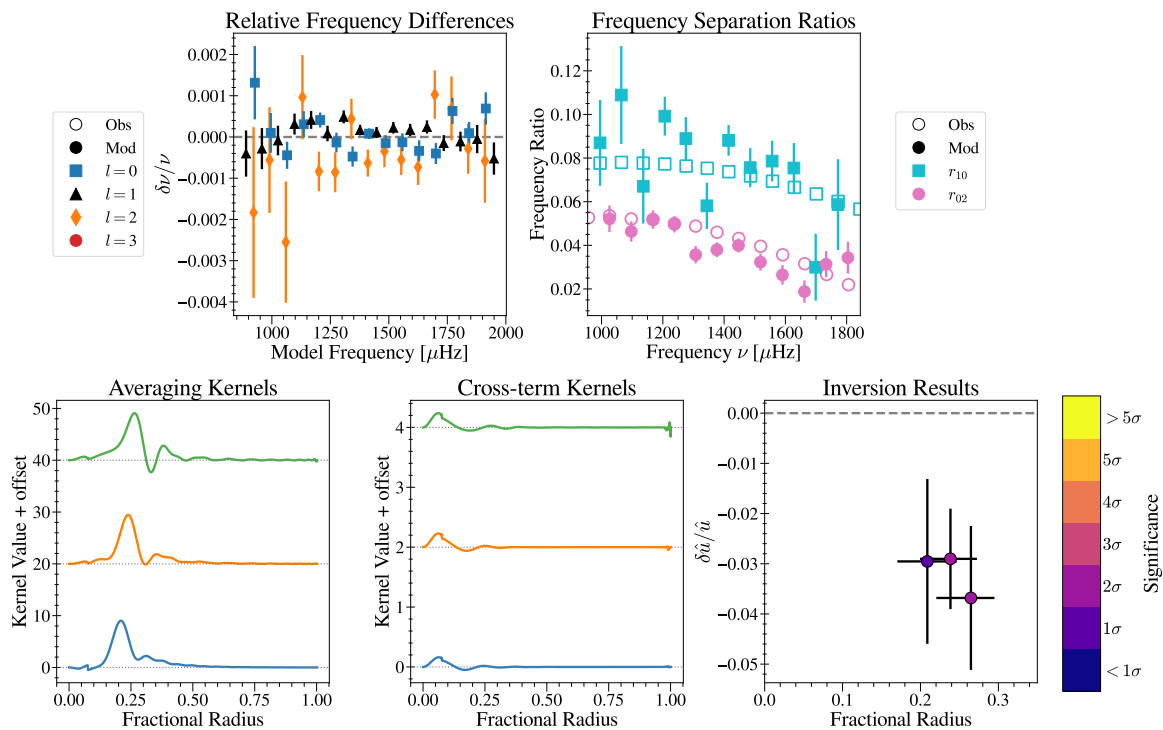


Figure 8. Modeling and inversion results for KIC 1435467. The top row shows the relative frequency differences after correcting for surface effects (left) and the frequency separation ratios (right). The model ratios are computed before the frequencies are corrected for surface effects. The bottom row plots the averaging kernels (left), cross-term kernels (center), and inversion results (right). Note that the y -axis scale differs between the left and center plots. The complete figure set (43 images) is available in the online journal.

REFERENCES

- Angelou, G. C., Bellinger, E. P., Hekker, S., et al. 2020, *MNRAS*, 493, 4987, doi: [10.1093/mnras/staa390](https://doi.org/10.1093/mnras/staa390)
- Angulo, C., Arnould, M., Rayet, M., et al. 1999, *NuPhA*, 656, 3, doi: [10.1016/S0375-9474\(99\)00030-5](https://doi.org/10.1016/S0375-9474(99)00030-5)
- Backus, G., & Gilbert, F. 1968, *Geophysical Journal*, 16, 169, doi: [10.1111/j.1365-246X.1968.tb00216.x](https://doi.org/10.1111/j.1365-246X.1968.tb00216.x)
- . 1970, *Philosophical Transactions of the Royal Society of London Series A*, 266, 123, doi: [10.1098/rsta.1970.0005](https://doi.org/10.1098/rsta.1970.0005)
- Ball, W. H., & Gizon, L. 2014, *A&A*, 568, A123, doi: [10.1051/0004-6361/201424325](https://doi.org/10.1051/0004-6361/201424325)
- Basu, S. 2003, *Ap&SS*, 284, 153
- . 2016, *Living Reviews in Solar Physics*, 13, 2, doi: [10.1007/s41116-016-0003-4](https://doi.org/10.1007/s41116-016-0003-4)
- Basu, S., & Chaplin, W. J. 2017, *Asteroseismic Data Analysis: Foundations and Techniques*
- Bellinger, E. P., Angelou, G. C., Hekker, S., et al. 2016, *ApJ*, 830, 31, doi: [10.3847/0004-637X/830/1/31](https://doi.org/10.3847/0004-637X/830/1/31)
- Bellinger, E. P., Basu, S., & Hekker, S. 2020, in *Astrophysics and Space Science Proceedings*, Vol. 57, *Dynamics of the Sun and Stars; Honoring the Life and Work of Michael J. Thompson*, ed. M. J. P. F. G. Monteiro, R. A. García, J. Christensen-Dalsgaard, & S. W. McIntosh, 171–183, doi: [10.1007/978-3-030-55336-4_25](https://doi.org/10.1007/978-3-030-55336-4_25)
- Bellinger, E. P., Basu, S., Hekker, S., & Ball, W. H. 2017, *ApJ*, 851, 80, doi: [10.3847/1538-4357/aa9848](https://doi.org/10.3847/1538-4357/aa9848)
- Bellinger, E. P., Basu, S., Hekker, S., & Christensen-Dalsgaard, J. 2019, *ApJ*, 885, 143, doi: [10.3847/1538-4357/ab4a0d](https://doi.org/10.3847/1538-4357/ab4a0d)
- Bellinger, E. P., Basu, S., Hekker, S., Christensen-Dalsgaard, J., & Ball, W. H. 2021, *ApJ*, 915, 100, doi: [10.3847/1538-4357/ac0051](https://doi.org/10.3847/1538-4357/ac0051)
- Bétrisey, J., Eggenberger, P., Buldgen, G., Benomar, O., & Bazot, M. 2023, *A&A*, 673, L11, doi: [10.1051/0004-6361/202245764](https://doi.org/10.1051/0004-6361/202245764)
- Buchele, L., Bellinger, E. P., Hekker, S., et al. 2024, *ApJ*, 961, 198 (B24), doi: [10.3847/1538-4357/ad1680](https://doi.org/10.3847/1538-4357/ad1680)
- Buldgen, G., Bétrisey, J., Roxburgh, I. W., Vorontsov, S. V., & Reese, D. R. 2022a, *Frontiers in Astronomy and Space Sciences*, 9, 942373, doi: [10.3389/fspas.2022.942373](https://doi.org/10.3389/fspas.2022.942373)
- Buldgen, G., Farnir, M., Eggenberger, P., et al. 2022b, *A&A*, 661, A143, doi: [10.1051/0004-6361/202142001](https://doi.org/10.1051/0004-6361/202142001)
- Campilho, B., Deal, M., & Bossini, D. 2022, *A&A*, 659, A162, doi: [10.1051/0004-6361/202140821](https://doi.org/10.1051/0004-6361/202140821)
- Christensen-Dalsgaard, J. 2021, *Living Reviews in Solar Physics*, 18, 2, doi: [10.1007/s41116-020-00028-3](https://doi.org/10.1007/s41116-020-00028-3)
- Chugunov, A. I., Dewitt, H. E., & Yakovlev, D. G. 2007, *PhRvD*, 76, 025028, doi: [10.1103/PhysRevD.76.025028](https://doi.org/10.1103/PhysRevD.76.025028)
- Cox, J. P., & Giuli, R. T. 1968, *Principles of stellar structure*
- Creevey, O. L., Sordo, R., Pailler, F., et al. 2023, *A&A*, 674, A26, doi: [10.1051/0004-6361/202243688](https://doi.org/10.1051/0004-6361/202243688)
- Creevey, O. L., Sordo, R., Pailler, F., et al. 2023, *Astronomy & Astrophysics*, 674, A26, doi: [10.1051/0004-6361/202243688](https://doi.org/10.1051/0004-6361/202243688)
- Cunha, M. S., Roxburgh, I. W., Aguirre Børsen-Koch, V., et al. 2021, *MNRAS*, 508, 5864, doi: [10.1093/mnras/stab2886](https://doi.org/10.1093/mnras/stab2886)
- Cyburt, R. H., Amthor, A. M., Ferguson, R., et al. 2010, *ApJS*, 189, 240, doi: [10.1088/0067-0049/189/1/240](https://doi.org/10.1088/0067-0049/189/1/240)
- Davies, G. R., Silva Aguirre, V., Bedding, T. R., et al. 2016, *MNRAS*, 456, 2183, doi: [10.1093/mnras/stv2593](https://doi.org/10.1093/mnras/stv2593)
- Deal, M., Alecian, G., Lebreton, Y., et al. 2018, *A&A*, 618, A10, doi: [10.1051/0004-6361/201833361](https://doi.org/10.1051/0004-6361/201833361)
- Deal, M., Goupil, M. J., Cunha, M. S., et al. 2023, *A&A*, 673, A49, doi: [10.1051/0004-6361/202245103](https://doi.org/10.1051/0004-6361/202245103)
- Ferguson, J. W., Alexander, D. R., Allard, F., et al. 2005, *ApJ*, 623, 585, doi: [10.1086/428642](https://doi.org/10.1086/428642)
- Fuller, G. M., Fowler, W. A., & Newman, M. J. 1985, *ApJ*, 293, 1, doi: [10.1086/163208](https://doi.org/10.1086/163208)
- Furlan, E., Ciardi, D. R., Cochran, W. D., et al. 2018, *The Astrophysical Journal*, 861, 149, doi: [10.3847/1538-4357/aaca34](https://doi.org/10.3847/1538-4357/aaca34)
- Gaia Collaboration, Prusti, T., de Bruijne, J. H. J., et al. 2016, *A&A*, 595, A1, doi: [10.1051/0004-6361/201629272](https://doi.org/10.1051/0004-6361/201629272)
- Gaia Collaboration, Brown, A. G. A., Vallenari, A., et al. 2018, *A&A*, 616, A1, doi: [10.1051/0004-6361/201833051](https://doi.org/10.1051/0004-6361/201833051)
- Gough, D. O. 1993, in *Astrophysical Fluid Dynamics - Les Houches 1987*, 399–560
- Gough, D. O., & Thompson, M. J. 1991, in *Solar Interior and Atmosphere*, 519–561
- Grevesse, N., & Sauval, A. J. 1998, *SSRv*, 85, 161, doi: [10.1023/A:1005161325181](https://doi.org/10.1023/A:1005161325181)
- Iglesias, C. A., & Rogers, F. J. 1993, *ApJ*, 412, 752, doi: [10.1086/172958](https://doi.org/10.1086/172958)
- . 1996, *ApJ*, 464, 943, doi: [10.1086/177381](https://doi.org/10.1086/177381)
- Irwin, A. W. 2004, *The FreeEOS Code for Calculating the Equation of State for Stellar Interiors*. <http://freeeos.sourceforge.net/>
- Itoh, N., Hayashi, H., Nishikawa, A., & Kohyama, Y. 1996, *ApJS*, 102, 411, doi: [10.1086/192264](https://doi.org/10.1086/192264)
- Jermyn, A. S., Schwab, J., Bauer, E., Timmes, F. X., & Potekhin, A. Y. 2021, *ApJ*, 913, 72, doi: [10.3847/1538-4357/abf48e](https://doi.org/10.3847/1538-4357/abf48e)
- Jermyn, A. S., Bauer, E. B., Schwab, J., et al. 2022, *arXiv e-prints*, arXiv:2208.03651. <https://arxiv.org/abs/2208.03651>

- . 2023, *ApJS*, 265, 15, doi: [10.3847/1538-4365/acae8d](https://doi.org/10.3847/1538-4365/acae8d)
- Kiefer, R., & Broomhall, A.-M. 2020, *MNRAS*, 496, 4593, doi: [10.1093/mnras/staa1807](https://doi.org/10.1093/mnras/staa1807)
- Kosovichev, A. G. 1999, *Journal of Computational and Applied Mathematics*, 109, 1
- Kosovichev, A. G., & Kitiashvili, I. N. 2020, in *Solar and Stellar Magnetic Fields: Origins and Manifestations*, ed. A. Kosovichev, S. Strassmeier, & M. Jardine, Vol. 354, 107–115, doi: [10.1017/S1743921320001416](https://doi.org/10.1017/S1743921320001416)
- Kuhfuss, R. 1986, *A&A*, 160, 116
- Langanke, K., & Martínez-Pinedo, G. 2000, *Nuclear Physics A*, 673, 481, doi: [10.1016/S0375-9474\(00\)00131-7](https://doi.org/10.1016/S0375-9474(00)00131-7)
- Lebreton, Y., & Goupil, M. J. 2012, *A&A*, 544, L13, doi: [10.1051/0004-6361/201220000](https://doi.org/10.1051/0004-6361/201220000)
- Lund, M. N., Silva Aguirre, V., Davies, G. R., et al. 2017, *ApJ*, 835, 172, doi: [10.3847/1538-4357/835/2/172](https://doi.org/10.3847/1538-4357/835/2/172)
- Mathur, S., Huber, D., Batalha, N. M., et al. 2017, *The Astrophysical Journal Supplement Series*, 229, 30, doi: [10.3847/1538-4365/229/2/30](https://doi.org/10.3847/1538-4365/229/2/30)
- Michaud, G., Alecian, G., & Richer, J. 2015, *Atomic Diffusion in Stars*, doi: [10.1007/978-3-319-19854-5](https://doi.org/10.1007/978-3-319-19854-5)
- Moedas, N., Bossini, D., Deal, M., & Cunha, M. S. 2024, *A&A*, 684, A113, doi: [10.1051/0004-6361/202348506](https://doi.org/10.1051/0004-6361/202348506)
- Moedas, N., Deal, M., Bossini, D., & Campilho, B. 2022, *A&A*, 666, A43, doi: [10.1051/0004-6361/202243210](https://doi.org/10.1051/0004-6361/202243210)
- Morel, T., Creevey, O. L., Montalbán, J., Miglio, A., & Willett, E. 2021, *Astronomy & Astrophysics*, 646, A78, doi: [10.1051/0004-6361/202039212](https://doi.org/10.1051/0004-6361/202039212)
- Noll, A., & Deheuvels, S. 2023, *A&A*, 676, A70, doi: [10.1051/0004-6361/202245710](https://doi.org/10.1051/0004-6361/202245710)
- Nsamba, B., Campante, T. L., Monteiro, M. J. P. F. G., et al. 2018, *MNRAS*, 477, 5052, doi: [10.1093/mnras/sty948](https://doi.org/10.1093/mnras/sty948)
- Oda, T., Hino, M., Muto, K., Takahara, M., & Sato, K. 1994, *Atomic Data and Nuclear Data Tables*, 56, 231, doi: [10.1006/adnd.1994.1007](https://doi.org/10.1006/adnd.1994.1007)
- Paxton, B., Bildsten, L., Dotter, A., et al. 2011, *ApJS*, 192, 3, doi: [10.1088/0067-0049/192/1/3](https://doi.org/10.1088/0067-0049/192/1/3)
- Paxton, B., Cantiello, M., Arras, P., et al. 2013, *ApJS*, 208, 4, doi: [10.1088/0067-0049/208/1/4](https://doi.org/10.1088/0067-0049/208/1/4)
- Paxton, B., Marchant, P., Schwab, J., et al. 2015, *ApJS*, 220, 15, doi: [10.1088/0067-0049/220/1/15](https://doi.org/10.1088/0067-0049/220/1/15)
- Paxton, B., Schwab, J., Bauer, E. B., et al. 2018, *ApJS*, 234, 34, doi: [10.3847/1538-4365/aaa5a8](https://doi.org/10.3847/1538-4365/aaa5a8)
- Paxton, B., Smolec, R., Schwab, J., et al. 2019, *ApJS*, 243, 10, doi: [10.3847/1538-4365/ab2241](https://doi.org/10.3847/1538-4365/ab2241)
- Pijpers, F. P. 2006, *Methods in helio- and asteroseismology*
- Rogers, F. J., & Nayfonov, A. 2002, *ApJ*, 576, 1064, doi: [10.1086/341894](https://doi.org/10.1086/341894)
- Roxburgh, I. W., & Vorontsov, S. V. 2003, *A&A*, 411, 215, doi: [10.1051/0004-6361:20031318](https://doi.org/10.1051/0004-6361:20031318)
- Salabert, D., Régulo, C., Pérez Hernández, F., & García, R. A. 2018, *A&A*, 611, A84, doi: [10.1051/0004-6361/201731714](https://doi.org/10.1051/0004-6361/201731714)
- Santos, A. R. G., Campante, T. L., Chaplin, W. J., et al. 2018, *ApJS*, 237, 17, doi: [10.3847/1538-4365/aac9b6](https://doi.org/10.3847/1538-4365/aac9b6)
- Saumon, D., Chabrier, G., & van Horn, H. M. 1995, *ApJS*, 99, 713, doi: [10.1086/192204](https://doi.org/10.1086/192204)
- Silva Aguirre, V., Davies, G. R., Basu, S., et al. 2015, *MNRAS*, 452, 2127, doi: [10.1093/mnras/stv1388](https://doi.org/10.1093/mnras/stv1388)
- Silva Aguirre, V., Lund, M. N., Antia, H. M., et al. 2017, *ApJ*, 835, 173, doi: [10.3847/1538-4357/835/2/173](https://doi.org/10.3847/1538-4357/835/2/173)
- Sobol', I. 1967, *USSR Computational Mathematics and Mathematical Physics*, 7, 86, doi: [https://doi.org/10.1016/0041-5553\(67\)90144-9](https://doi.org/https://doi.org/10.1016/0041-5553(67)90144-9)
- Thompson, M. J., & Christensen-Dalsgaard, J. 2002, in *ESA Special Publication*, Vol. 485, *Stellar Structure and Habitable Planet Finding*, ed. B. Battrick, F. Favata, I. W. Roxburgh, & D. Galadi, 95–101. <https://arxiv.org/abs/astro-ph/0110447>
- Townsend, R. H. D., & Teitler, S. A. 2013, *MNRAS*, 435, 3406, doi: [10.1093/mnras/stt1533](https://doi.org/10.1093/mnras/stt1533)
- Verma, K., Raodeo, K., Antia, H. M., et al. 2017, *ApJ*, 837, 47, doi: [10.3847/1538-4357/aa5da7](https://doi.org/10.3847/1538-4357/aa5da7)
- Verma, K., & Silva Aguirre, V. 2019, *MNRAS*, 489, 1850, doi: [10.1093/mnras/stz2272](https://doi.org/10.1093/mnras/stz2272)
- Zhang, J. 2020, *MNRAS*, 497, 4042, doi: [10.1093/mnras/staa2199](https://doi.org/10.1093/mnras/staa2199)